

FEDSM-ICNMM2010-30218

A VISUALIZATION STUDY DURING FLOW BOILING OF R134a IN A HORIZONTAL MICROCHANNEL

Rashid ALI
rashid.ali@energy.kth.se

Björn PALM*
bpalm@energy.kth.se

Mohammad H. MAQBOOL
maqbool@kth.se

Applied Thermodynamics and Refrigeration, Royal Institute of Technology, KTH
Brinellvägen 68, 100 44-SE, Stockholm, Sweden
*Tel: +46 (0)8 790 7453; Fax: +46 (0)8 20 41 61

ABSTRACT

In this paper, the experimental flow boiling visualization results of a microchannel are presented and discussed. A series of visualization experiments have been conducted in a horizontal, circular, uniformly heated microchannel, to record the two-phase flow patterns evolved during the boiling process and to study the ebullition process. A high speed camera (REDLAKE HG50LE) with a maximum of 100000 fps together with tungsten lights was used to capture the images along the test section. Microchannel was made of circular fused silica tube having an internal diameter of 0.781 mm and a uniformly heated length of 191 mm. Outside of the test tube was coated with a thin, electrically conductive layer of Indium Tin Oxide (ITO) for direct heating of the test section. Refrigerant R134a was used as working fluid and experiments were performed at two different system pressures corresponding to saturation temperatures of 25 °C and 30 °C. Mass flux was varied from 100 kg/m²s to 400 kg/m²s and heat flux ranged from 5 kW/m² to 45 kW/m². Visualization results show that the bubble growth is restricted by the tube diameter which results in very short existence of isolated bubbly flow regime except essentially restricted to a very short length of test tube. Flow patterns observed along the length were: Isolated bubble, elongated bubble, slug flow, semi annular and annular flow. Rigorous boiling and increased coalescence rates were observed with increase in heat flux. Bubble frequency was observed to increase with both heat and mass flux. A comparison with our previous flow boiling visualization studies, carried out for a test tube of 1.33 mm internal diameter, shows that the number of active nucleation sites is less while the bubble frequency is higher for the current study. Mean bubble length and bubble velocity during elongated bubble flow pattern have also been calculated from the images obtained during the tests.

Keywords: Microchannels, Two-phase, Flow patterns, Heat Transfer, visualization

1. INTRODUCTION

Micro/Minichannel heat sink with flow boiling has emerged as competitive and potential option for high heat flux cooling applications. Microchannels offer several advantages such as reduced inventory of fluid, low weight, reduced cost (due to reduced material requirements and advanced micro manufacturing technologies available). There could be several application areas for microchannel heat sinks such as cooling of electronics, automotive heat exchangers, cryogenics, commercial refrigeration and air conditioning just to mention a few. Compactness and reduced fluid inventory are very attractive benefits offered by the microchannels which can be exploited for enhancing the safety of heat exchange equipment and for meeting the ever increasing concerns of the environmental pollution. Advances in fuel-cell technology also require the design of compact and enhanced micro heat exchange devices.

In recent years, tremendous efforts have been devoted to understand the basic phenomenon involved during the boiling of fluids in microchannels. Two-phase heat transfer, pressure drop and critical heat flux (CHF) are believed to be flow pattern dependent and are essential parameters to be predicted as accurate as possible for the optimum design of micro heat exchange devices. It is known that reducing the channel diameter in a heat exchanger may enhance heat transfer [1] and the designers for compact heat exchangers may use hit and trial to select a suitable geometry and diameter for enhanced heat transfer but the fundamental mechanisms responsible for enhanced heat transfer during flow boiling in micro scale geometries are less known. Despite the great efforts made by

researchers to model the flow boiling heat transfer, CHF and pressure drop in microchannels, the basic mechanisms involved are still subject to further investigations. Flow visualization may greatly help in understanding the actual physics behind the heat transfer and flow boiling process. It is, therefore, essentially required to conduct more flow boiling visualization experiments to understand the basic physics involved during the two-phase flow process and to provide optimum design tools for micro heat exchange devices.

It is more relevant here to state that in open literature; it seems that most of the visualization experiments carried out for microchannels are for adiabatic two-phase flow or for air-water systems. Flow patterns evolved during the boiling process could be different than those formed during adiabatic flow process. It will, therefore, be interesting to conduct experiments in which the bubble generation is caused by the heating of the conduit itself.

Kuo et al [2] experimentally investigated the bubble dynamics during flow boiling of deionised water in enhanced surface microchannels with 0.227 mm hydraulic diameter. Key features of nucleate boiling such as active nucleation site density, bubble diameter, bubble frequency, and flow patterns were reported and discussed. Mass flux and heat flux range during the experiments was 41 to 302 kg/m²s and 28 W/cm² to 445 W/cm² respectively. Bubbly, slug and annular flow patterns were identified in the experiments. Nucleation sites were observed to shift to inlet region with increase in heat flux while the product of bubble frequency and diameter was observed to be lower than conventional channels.

Revellin et al [3] experimentally investigated the length and velocity of elongated bubbles in a 0.5 mm microchannel and using R134a as a working fluid at three different system pressures corresponding to saturation temperatures of 26, 30 and 35 °C. The experimental conditions were: mass flux from 323 kg/m²s to 1986 kg/m²s, inlet subcooling degree from 2 to 5 °C, heat flux from 4.7 to 81.3 kW/m² and exit vapour quality from 0.005 to 0.22. The elongated bubble velocity and length were observed to increase with increase in vapour quality and decrease in saturation temperature. Inlet subcooling was seen to have no effect on bubble velocity and length within the range of inlet subcooling covered during experiments.

Saturated flow boiling experiments were performed by Owhaib et al [4] in a vertical minchannel of 1.33 mm internal diameter and 235.5 mm in heated length. Experiments were performed at a system pressure of 6.425 bar using R134a as working fluid. Other experimental conditions included: mass flux from 29 to 202 kg/m²s, heat flux from 5 to 20 kW/m². Experimental results indicated that the bubble frequency increased with mass flux. It was observed that the bubble departure diameter decreased with mass flux and bubble frequency was found to be higher at higher heat flux.

Celata et al [5] carried out an experimental study to analyze the flow patterns evolved in 4 mm and 6 mm inner diameter tubes under microgravity conditions. The test tube was made of Pyrex glass and the working fluid used was FC-72. Experimentally observed flow patterns were: bubbly, plug and churn flow. They observed that the vapour bubbles at micro gravity and low mass flow rates were larger than those observed under normal gravity conditions. Experimental flow

patterns were compared with existing flow pattern maps developed for micro and normal gravity conditions and suggestions were correspondingly made to improve the flow map of Dukler et al.

Coleman and Garimella [6] experimentally investigated the effect of channel shape and diameter on flow patterns during co-current flow of air-water mixtures in horizontal circular and rectangular channels. Round tubes having inner diameters from 1.3 mm to 5.5 mm and rectangular tubes with same hydraulic diameters and aspect ratio of 1 were tested. Experimental flow pattern maps were presented in the form of superficial liquid and gas velocities and the same were compared with flow pattern maps existing in the literature. Superficial liquid velocity ranged from 0.1 to 100 m/s and superficial gas velocity ranged from 0.01 to 10 m/s. The authors observed that the stratified flow was suppressed and the intermittent flow was observed to occur at higher superficial liquid velocities in small diameter tubes due to the effect of surface tension and decrease in tube diameter.

Yang et al [7] used advanced numerical simulation method to investigate the movement of Taylor bubbles in narrow channels. They also investigated the liquid film thickness between the tube wall and the bubble and used Bretherton [8] correlation to compare their numerical simulation results and found a reasonable agreement. More recently, the studies have been performed by Han and Shikazono [9-10] to investigate experimentally the liquid film thickness in slug flow. The authors also presented correlations for the calculation of liquid film thickness.

In the present study, experiments have been performed with a single, circular, horizontal microchannel with internal diameter of 0.781 mm and a uniformly heated length of 191 mm using refrigerant R-134a as working fluid. Test tube was made of fused silica outside of which was coated with very thin, electrically conductive layer of Indium-Tin-Oxide (ITO) for direct heating of test section. Direct heating of the test tube ensured that the flow patterns evolved during the experiments were due to actual boiling process taking place in the test section unlike those involving water-air mixtures to create two-phase flows. Flow patterns have been recorded using a high speed camera together with tungsten lights. The camera was provided with close up lens to get the required magnification and to obtain improved spatial and temporal resolution. Number of nucleation sites, bubble frequency, elongated bubble length, elongated bubble velocity have been calculated at different heat and mass flux conditions.

2. DESCRIPTION OF THE EXPERIMENTS

2.1 Experimental apparatus and data reduction

A schematic diagram of the test rig is shown in figure 1. The test facility was supplied with instruments as shown in the figure 1 and explained below. The design of the facility was such that the system pressure, heat flux, mass flux and inlet sub cooling degree could be adjusted independently. Circulation of the fluid was driven by a magnetic gear pump with microprocessor control, type ISMATEC MCP-Z standard, and was measured with a Coriolis Effect mass flow

meter. The pump could be run in different modes and gave a wide variety of flow rates depending upon the type of head used. The evaporation temperature was defined by the system pressure, which was controlled by adjusting the flow rate of the cooling water through the condenser. Further fine control and maintenance of the system pressure was achieved by adjusting the liquid level in the condenser by controlling the electrical heat input to a refrigerant tank connected to the main loop. Sub cooling degree at the inlet of the test section was adjusted by controlling the electrical heat input to the preheater located just before the test section. A $7\ \mu\text{m}$ filter was used in the loop to prevent any small particles from entering the test section.

Test facility was instrumented with an absolute pressure transducer (Druck, 20 bar) to measure the pressure at the inlet of the test section and a differential pressure transducer (Druck, 350 mbar) to measure the pressure drop across the test section. Apart from the thermocouples attached to the test section, some thermocouples were inserted at different locations in the experimental setup to measure the fluid bulk temperature. The entire test rig was properly insulated to minimize the heat losses.

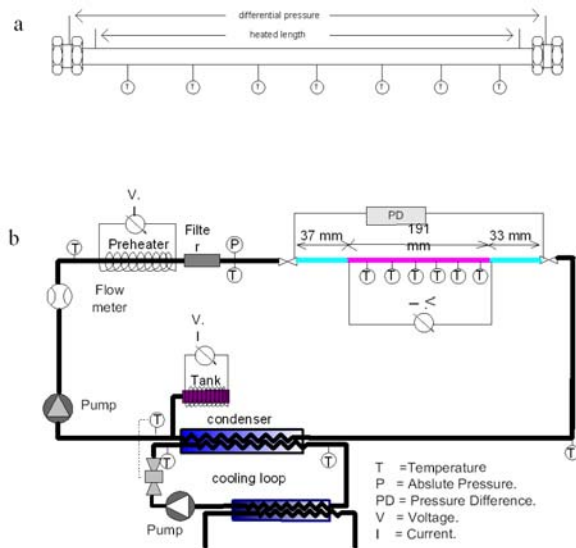


Fig 1 (a) Details of the test section (b) Schematic diagram of experimental set up

A high-speed CMOS digital camera (Redlake HG50LE) with a maximum frame rate of 100000 together with tungsten lights was used for the visualization study of flow boiling of R134a along the test section. Close up lens was used with the camera to get the required magnification and obtain good spatial and temporal resolution for studying the bubble dynamics. Flow patterns were recorded at 1000 to 5000 fps at different positions along the test section. Images were taken at the thermocouple positions or just at the middle of any of the two thermocouple positions as shown in the figure 1. Appropriate lighting intensity and conditions were first set to obtain good quality images.

The test tube was made of fused silica with an internal diameter of 0.781 mm and a total length of 261 mm with 191 mm of heated length. Internal surface structure of the test tube was scanned using the method of stylus profilometry to obtain the surface roughness information and calculated arithmetic mean roughness R_a value was found to be $0.015\ \mu\text{m}$ with a maximum valley depth of $0.036\ \mu\text{m}$. Scanning image of the inner surface can be viewed in figure 2, where it is observed that the inner surface is quite smooth, as expected for a glass tube. Seven thermocouples, which were calibrated using an ice bath (mixture of ice and water), were glued on the outer surface of the tube using an electrically insulating and thermally conductive epoxy. Swage lock with brass connections was used at two ends of the test section to connect it to main loop. Two holes on brass connections just at the inlet and outlet of the test section were drilled for pressure taps as shown in the figure 1a.

Single phase friction factor was calculated as

$$f = \frac{64}{\text{Re}} \quad \text{For laminar flow } \text{Re} < 2300$$

$$f = 0.3164 \times \text{Re}^{-0.25} \quad \text{For Turbulent flow } \text{Re} > 2300$$

Where Re is Reynolds number defined as

$$\text{Re} = \frac{GD}{\mu}$$

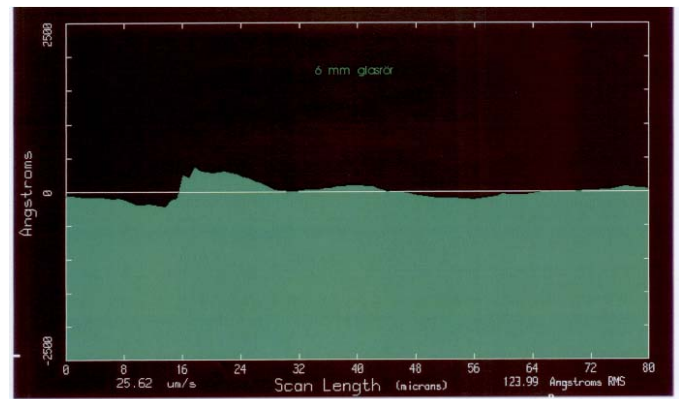


Fig 2 Scanning image of the inner surface of the test tube

For a given test point, the heat flux added to the test section q'' was calculated as

$$q'' = \frac{Q - Q_{\text{loss}}}{A}$$

$$Q = I \times V$$

Where I and V are current and voltage in ampere and volts respectively and A is the heat transfer area given as $A = \pi DL_h$. Q_{loss} is heat loss to the ambient which was calculated by heating the test section without pumping the fluid. When the

wall temperatures became constant, the power was noted. This procedure was repeated and finally the power loss was correlated with the temperature difference between wall and the ambient for different values of power and wall temperature. A Yokogawa WT130 power meter was used to measure the voltage and current applied to the test section.

The thermodynamic vapour quality at any axial position $x_{th}(z)$ was calculated from the heat transferred to the fluid as,

$$x_{th} = \frac{q'' \pi D (z - z_{sat})}{A_c G i_{lg}}$$

Where D is the internal diameter of the test tube, z is any axial location, z_{sat} is the location where boiling starts (i.e. saturated conditions are reached), A_c is the cross sectional area of the test tube, G is the mass flux and i_{lg} is the latent heat of vaporization. Axial position where saturated conditions are reached can be calculated as [11]

$$z_{sat} = \frac{m c_p (T_{sat} - T_{in})}{q'' \pi D}$$

Where m is the mass flow rate, C_p is the specific heat of the fluid, T_{in} is the inlet temperature at the test section and D is the diameter.

Total pressure drop in the test section is the sum of two-phase frictional pressure drop, momentum pressure drop and single phase pressure drop from inlet up to the position where boiling starts i.e. z_{sat}

$$\Delta P_{tot} = \Delta P_{sp} + \Delta P_{tp} + \Delta P_m$$

2.2 Experimental method

Experiments were performed at two system pressures corresponding to $T_{sat}=25$ °C and $T_{sat}=30$ °C. System pressure, mass flow rate, inlet temperature were first set to a desired level and then heat flux was applied in small steps to start the boiling in the test section. Before taking each data point, sufficient time was given to the system to achieve the steady state particularly to achieve stable temperatures over the test section. When the steady state was achieved, more than 100 data points of each parameter, such as system pressure, differential pressure, wall temperatures, mass flow rate, fluid temperature at different locations, were recorded using a HP data logger with a frequency of 0.3 Hz and the average value of the parameters recorded was used in the calculations. The data logger was connected to a personal computer and a computer programme written in HP VEE was used to display and obtain the real time data in a excel sheet for further processing. Thermo-physical and transport properties of the refrigerant were obtained with REFPROP 7.0 developed by National Institute of standards and Technology (NIST) [12]. The use of transparent tube together with ITO coating allowed simultaneous visualization and electrical heating. Flow patterns were recorded at six positions along the tube. Pictures taken with the camera were transferred to a PC and later

processed to identify the flow patterns and obtain other information like number of nucleation sites, bubble frequency and bubble velocity etc.

Table 1 Operating parameters and uncertainties

Parameter	Range	Uncertainty
D [mm]	0.781	0.004
G [kg/m ² s]	100-400	±2%
q'' [kw/m ²]	7 to 45	±3%
T _{sat} [°C]	25, 30	±0.2
ΔT _{sub,in} [°C]	2 for T _{sat} =25 °C 6 for T _{sat} =30 °C	±0.2
x _{th} [-]	0.005 to 0.95	±5%

2.3 Uncertainty analysis

Uncertainty analysis was performed for all the data points by the method as given by Moffat [13]. From the uncertainties in the measurements of tube diameter, tube length, power input, temperature, pressure and mass flow rate, the uncertainties of the derived parameters including the heat flux, mass flux, and vapour quality were estimated. Two coriolis mass flow meters were installed in the loop and one of the two was used depending upon the mass flow rate of the refrigerant. The mass flow meter used for small flow rates has an accuracy of 0.2% while the one used for higher flow rates (only in case of single phase tests with Reynolds number greater than 2000) has an accuracy of 0.5%. Hence, in the case of two-phase tests the accuracy of mass flow rate was always very good. The thermocouples were calibrated using ice water mixture and were found to have a calibrated accuracy of ±0.1 °C. The absolute pressure transducer has an accuracy of ±0.5% of full scale. The differential pressure transducer (Druck PDCR 4160, 0-350 mbar differential) was used with an accuracy of ±0.05% of full scale. For single phase tests the heat balance on the test section was, in the worst case, up to ±8% but in most of the cases it was within ±5%. The Yokogawa power meter used for measurements has an accuracy of 0.25%. The overall uncertainty in the effective power (the difference between applied power and power loss) was estimated to be less than 3%. The heat flux had a maximum estimated uncertainty of ±3%. The uncertainty in vapour fraction was estimated to be ±5%. The uncertainty in mean bubble length and mean bubble velocity was determined from the blur or distortion in the image and on the face and tail of the elongated bubble. The idea was to not only detect the edge of the bubble but also allow for the uncertainty in positioning of the face or tail of the bubble due to blur. The uncertainty in mean bubble velocity thus estimated was from 10 to 15 % depending up on blur and resolution of the image. Experimental parameters and operating conditions are summarised in Table 1.

3. EXPERIMENTAL RESULTS AND DISCUSSION

3.1 Flow patterns evolved during flow boiling

Flow patterns were identified from the videos obtained during the experiments. There seems to be no generally agreed flow patterns; rather different researchers identify the flow regimes differently. In the current experiments a distinction between intermittent and non-intermittent flow regimes can easily be made. Following are the distinct flow patterns identified by looking at the videos obtained.

Isolated bubble: Bubble diameter is smaller than the tube diameter. Bubble growth is not hindered by the tube walls. In addition there is enough space for evaporation at the liquid vapour interface. This flow regime is characterized with distinct and almost spherical bubbles. Bubbly flow regime was observed to prevail for very short lengths. After the onset of boiling, as the heat flux was increased, the nucleation sites shifted to upstream and ultimately at higher heat fluxes for a given mass flux, the bubbly flow was restricted at close to the inlet of the test section. For all mass fluxes this flow regime was only observed for very short lengths and in some situations confined bubble regime was observed immediately after the departure of the bubbles (almost direct transition to confined bubble regime).

Confined bubble: The bubbles soon after the departure from nucleation sites grow to the diameter comparable to the tube diameter and further growth of bubble is restricted by channel walls. Due to the hindrance in growth, the bubbles start growing in axial direction and as a consequence the bubbles are no more spherical.

Elongated bubble: Due to the small diameter of the channel, the confined bubbles occupy almost the entire cross-section of the microchannel and start growing in axial direction. In the current study we call this the elongated bubble. As the bubbles grow to size of the channel diameter, they leave behind a very thin liquid film which surrounds the elongated bubble and fills the gap between bubble and channel walls. In the current study if the length of the bubble is from slightly larger than the diameter of the channel up to 5 times the diameter, it is termed as elongated bubble.

Slug flow: As the length of elongated bubbles grows along the tube, the face of the trailing bubble meets the rear of the leading bubble to form large vapour plugs which is very large compared to elongated bubble. Liquid slugs or sometimes small liquid drops are present between two vapour plugs. The tail of vapour plugs is wavy and in many cases touching the upper or lower part of the channel as the flow proceeds along the tube. In the current study, the bubbles larger than $5D$ are considered to be slug flow regime.

Wavy annular/semi annular flow: Slug-annular and churn-annular flow patterns are included in semi annular flow regime. If transition to annular flow occurs through the slug flow (which is mostly true for low and medium mass fluxes in present tests) then the two large plugs meet to form the wavy annular flow and the tail of the plugs which is wavy creates waves in the liquid film which flows along the channel walls. Waves in both top and bottom liquid layers are observed. Occasionally, the annular flow regime is interrupted by very large vapour plugs.

Wavy annular flow is also reached through churn flow (at high mass fluxes). At increased mass fluxes usually annular flow is

disturbed periodically by chaotic waves of liquid originating somewhere upstream of the channel.

Annular flow: annular flow is characterized with a continuous liquid ring surrounding the channel walls. The thickness of the liquid film decreases with increase in vapour fraction along the tube. The thickness of the liquid film also decreases with an increase in heat flux at a given position. The vapour flows in channel core with very small liquid droplets entrained in the vapour core.

Annular mist flow: this is transitional flow regime between annular and mist flow where the mist flow is disturbed with flushing liquid coming from upstream. This liquid which flows at the channel walls is then evaporated and tube walls again become dry while some tiny liquid droplets flow in the centre of the channel.

Mist flow: characterized with tiny liquid drops flowing mainly as dispersed in the channel core while tube walls are blanketed with vapour. Heat transfer is mainly due to vapour in contact with tube walls and due to the liquid droplets hitting the wall.

Similar flow patterns were observed in our previous study [15] conducted for a single circular tube of 1.33 mm internal diameter and also by [16-18] amongst others.



(a) Isolated bubble



(b) Confined bubble



(c) Elongated bubble



(d) Slug flow



(e) Semi annular flow



(f) Wavy annular



(g) Annular

Fig 3 Flow patterns observed during flow boiling in the test section of $D=0.781$ mm

3.2 Nucleation sites and bubble frequency

The present study concerns a heat flux controlled system where heat was applied in small steps and keeping the mass flux constant. As the heat flux was increased, the wall superheat increased and at a certain point the natural cavities present in the test tube became active and boiling started somewhere close to the outlet of the tube. At higher heat fluxes the nucleation sites shifted towards upstream of the test section. When the flow regime changed along the test section from bubbly to elongated bubble and to annular flow, the nucleation sites active before became inactive and nucleation was restricted essentially to the inlet of the test section. Further increase of heat flux caused either vigorous boiling or increased the number of active nucleation sites. At very high heat fluxes, vigorous boiling and increased coalescence rates were observed which, in some cases, made it difficult to count the nucleation sites exactly. First images were captured at the point where boiling initiated afterwards as the boiling started in the whole test tube, the images were captured along the positions mentioned before i.e. at thermocouple positions. In the current study, active nucleation sites were counted by looking at the images taken during the flow boiling process. The bubble departure frequency was determined by counting the number of frames between bubble departures, and as the frame rate for the particular case was known, the frequency of the departing bubbles could be calculated. A plot of heat flux and number of active nucleation sites at different mass fluxes and system pressures is viewed in figure 4. For each mass flux, the number of active nucleation sites increases with heat flux up to a certain point except for $G=400 \text{ kg/m}^2 \text{ s}$ for which only one data point is available. A comparison to our previous flow boiling visualization study [4] for a test tube of $D=1.33 \text{ mm}$ shows that the number of active nucleation sites is less for the current study of 0.781 mm test tube for the same heat and mass flux conditions.

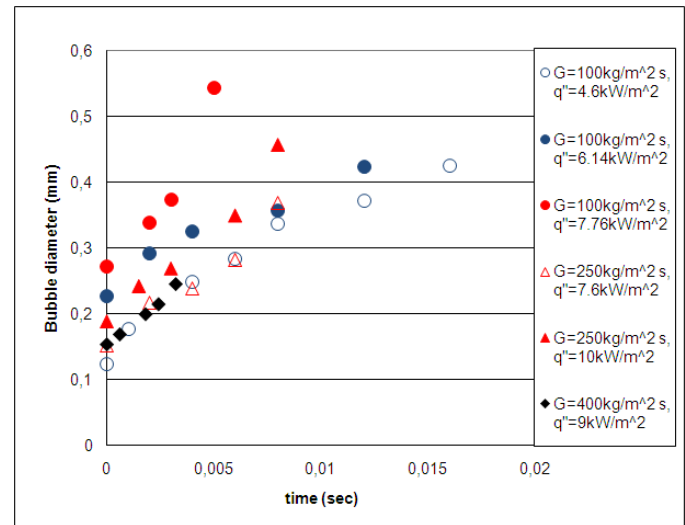


Fig 5 Bubble growth after detachment with time, $T_{\text{sat}}=25^\circ\text{C}$

Bubble growth after detachment with time for different heat and mass fluxes can be seen in figure 5. Due to insufficient magnification of the image and very quick growth, it was not possible to measure the bubble diameter before detachment. Therefore, the bubble diameter at time zero (detachment) is not zero. It may be observed from the figure 5 that for a given mass flux the bubble diameter also increases with heat flux. Except for $G=400 \text{ kg/m}^2 \text{ s}$ it may be observed that for a higher mass flux the bubble diameter is smaller for a given heat flux condition. Increasing the mass flux reduced the bubble departure diameter which is in agreement with our previous flow visualization study [4,19] and also with other studies present in the literature for example [2]. A possible reason for decrease in bubble departure diameter with mass flux is the increased drag force experienced by the nucleating bubbles. It may be commented here that the last data points in the case of $G=100 \text{ kg/m}^2 \text{ s}$, $q''=7.76 \text{ kW/m}^2$ and for both heat fluxes of $G=250 \text{ kg/m}^2 \text{ s}$, the bubbles coalesce with another bubble nucleating from the neighbouring active nucleation site. Therefore, the last data point in some of the cases is seen to slightly deviate from more or less linear growth of bubble before this point. Therefore, this deviation may be termed as the effect of coalescence of bubbles due to the increase in heat flux.

Bubble frequency has strong influence on heat transfer rate and is thus very important to determine. The bubble frequency was calculated as explained earlier in this section and can be viewed in figure 6. Bubble frequency increased with heat and mass flux. At higher mass fluxes the bubble departure diameter reduces due to drag force hence the bubbles depart at a higher frequency. For a given mass and heat flux condition, there are more than one active nucleation sites (in the same video) and bubble frequency is different for each nucleation site as can be seen in figure 6, which may be due to different size and shape of the natural cavities present

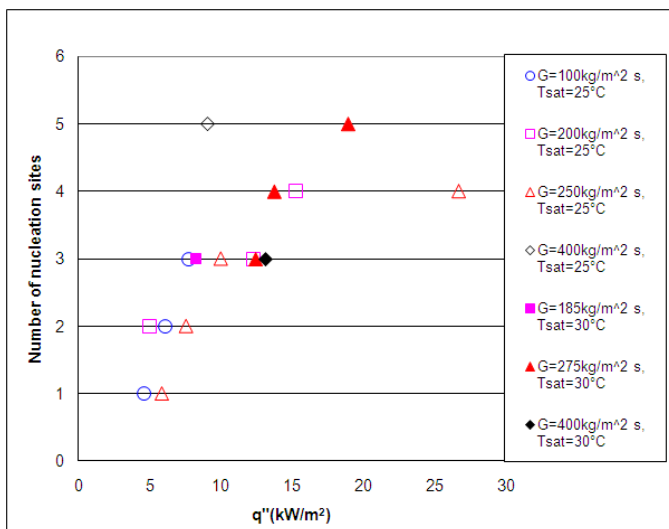


Fig 4 Number of active nucleation sites versus heat flux for different mass fluxes and two system pressures

on the surface. A comparison of present study with our previous study [4] carried out for 1.33 mm diameter test section shows that bubble frequency is higher for smaller diameter channel for the same operating conditions which will mean that the transition from bubble to slug will occur earlier and also the slug to annular transition will be expected to occur earlier for a smaller diameter channel.

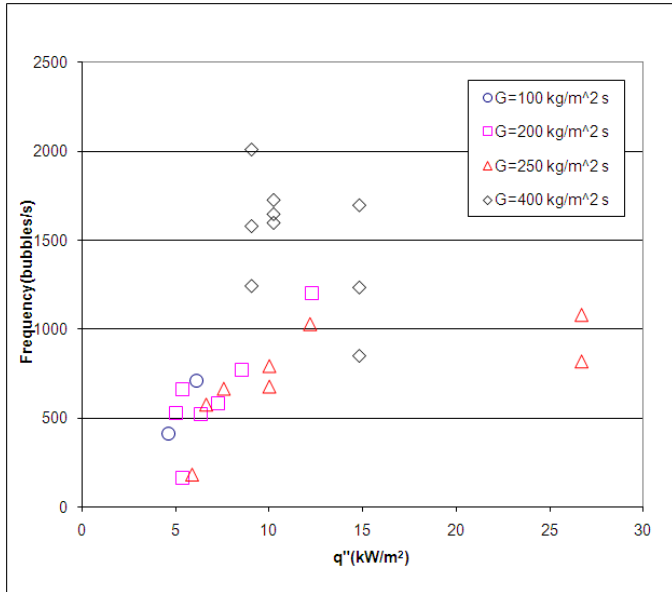


Fig 6 Bubble frequency versus heat flux for different mass fluxes, $T_{sat}=25\text{ }^{\circ}\text{C}$

Bubble frequency is strongly related to coalescence rate. As the bubble frequency increases with increasing heat flux, the coalescence rate also increases. This causes the successive flow regimes to occur earlier. In some cases of high heat fluxes, it was difficult to count bubble frequency due to quick coalescence of bubbles. It was observed that the two bubbles merged very quickly after the departure (merged very close to the nucleating site) and this might be a reason for low bubble frequency at higher heat flux for $G=250\text{ kg/m}^2\text{ s}$.

3.3 Elongated bubble regime

Elongated bubble regime is one of the basic flow regimes prevailing in microchannels. In microchannels elongated bubble is formed because of the confinement due to small channel dimensions. This is evident from current experiments and other microchannel visualization studies found in the literature. This also shows the growing importance of surface tension forces as the channel dimensions decrease. Special feature of this flow regime is the thin liquid layer existing between the elongated bubble and the channel wall. The evaporation of the thin liquid film is believed to enhance the heat transfer. In fact thin film evaporating between the bubble and the channel wall during flow boiling in microchannels is closely related to heat transfer mechanism in pool boiling and this idea is very helpful in developing models for heat transfer in microchannels. Measurement of thin liquid film is thus

critical in modelling of the heat transfer process. The length and the Velocity of elongated bubbles are also important parameters to be measured in order to get an insight of merger process. It would be reasonable to assume that the velocity of the elongated bubbles will increase with mass flux, vapour fraction and also with decreasing the system pressure. Experimental values of mean elongated bubble length and velocity were calculated from the images captured during the experiments. The procedure of calculating the length and velocity and the corresponding uncertainty of the elongated bubble is given below.

Consider figure 7a in which P_{face} and P_{tail} are pixel values at face and tail of the bubble respectively and P_{ref} is the reference scale pixels (pixels/mm) then the length of the elongated bubble in mm is given by

$$L = (P_{face} - P_{tail}) / P_{ref}$$

For calculating the velocity of the bubble consider figure 7b in which if P_i and P_f are the initial and final known pixels of the image, P_{ref} is the reference scale pixels as defined above, t is time in seconds then velocity is given as

$$v = (P_f - P_i) / (P_{ref} \times t)$$

Where time t is calculated as

$$t = N / \text{fps}$$

where fps are the frames per second of the high speed camera at which the images have been recorded and N is the number of frames taken by the elongated bubble to reach from initial pixel to final pixel position as shown in the figure 7b. A total of 5 to 20 bubbles were randomly selected to calculate the elongated bubble length and velocity and average of the values was calculated. Therefore, the plotted values in the following sections are the mean value of bubble length and velocity. The uncertainty in the length and velocity was calculated by taking into account the blur in the image both at face and tail of the bubble.

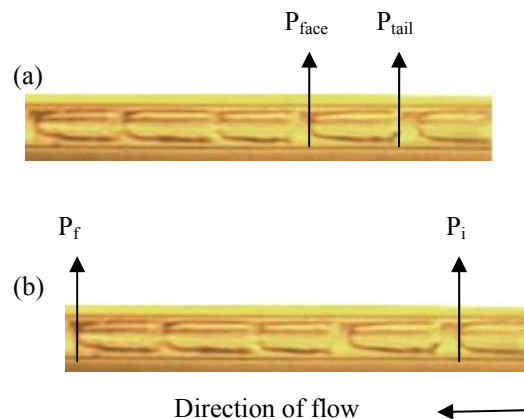


Fig 7 Illustration of calculation procedure of elongated bubble length and velocity

A plot of vapour fraction and mean elongated bubble velocity can be viewed in figure 8. It can be seen that the mean elongated bubble velocity increases with vapour fraction. A change in slope in figure 8 is observed for $G=275 \text{ kg/m}^2 \text{ s}$ and a vapour quality of about 0.12 which may be an indication of increased merger and a corresponding increase in slip rate due to increased vapour velocity and transition to next flow regime. This increased merger rate is also supported from the video of this specific mass flux and heat flux condition i.e. at $x=0.12$ which clearly revealed that further increase in vapour fraction along the test section (i.e. downstream of the test section) led to change of flow pattern to slug flow. The images for this point i.e. at $x=0.12$ were taken at a distance of 125 mm from inlet and the flow pattern recorded was elongated bubble where the length of the bubbles was approximately 3 times the tube diameter and the bubble velocity was 833 mm/s. While the next images at the same heat and mass flux condition were taken at a distance of 179 mm from the inlet of the tube (i.e. downstream of the tube) where the vapour fraction was 0.21 and the flow pattern changed from elongated bubble to slug flow and the length of the vapour plugs was approximately 35 times the tube diameter and the velocity was approximately 1200 mm/s. It was also experimentally shown by Agostini et al [20] that the relative elongated bubble velocity increased with bubble length. Keeping in view these observations that increased length and velocity facilitate the transition process to successive flow regime, it might be possible to define transition criteria for annular flow regime based on critical values of the length and the velocity of the elongated bubbles. It may be noted here that increase in heat flux at a given position along the tube also causes the increase in bubble length which also facilitates the coalescence process and hence transition to successive flow regime.

Length of the elongated bubbles is an important parameter which can be helpful in understanding the merger process. As the vapor quality along the channel increases, the elongated bubble length will also increase. Experimental values of the mean bubble length have been calculated from the videos obtained during the visualization process. Experimental values of elongated bubble length versus vapor quality obtained at two different system pressures corresponding to saturation temperatures of $T_{\text{sat}}=25 \text{ }^\circ\text{C}$ and $T_{\text{sat}}=30 \text{ }^\circ\text{C}$ are viewed in figure 9. As expected, the bubble length increases with vapor quality for both the system pressures. Experimental points for $T_{\text{sat}}=25 \text{ }^\circ\text{C}$ are not enough but it seems from the limited data points that bubble length for a lower system pressure is slightly larger for a given vapor quality.

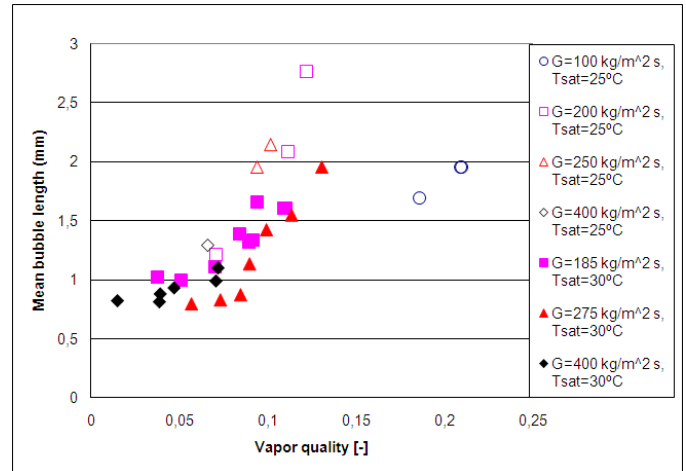


Fig 9 Mean length of elongated bubbles against vapor quality for different mass fluxes and at $T_{\text{sat}}=30 \text{ }^\circ\text{C}$ and $T_{\text{sat}}=25 \text{ }^\circ\text{C}$

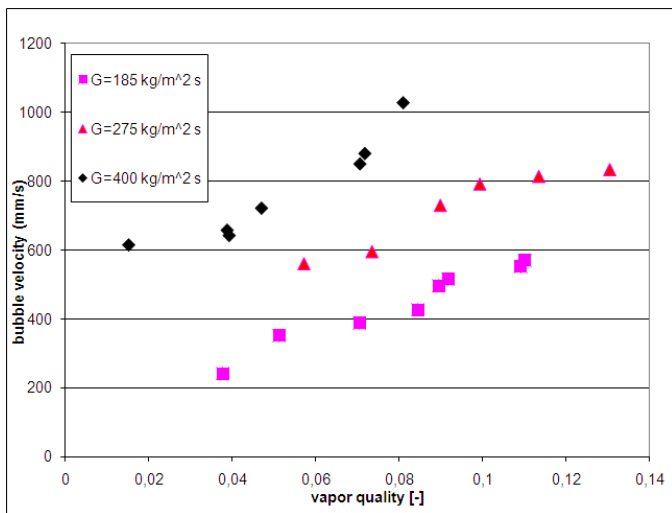


Fig 8 Mean velocity of elongated bubbles against vapor quality for different mass fluxes, $T_{\text{sat}}=30 \text{ }^\circ\text{C}$

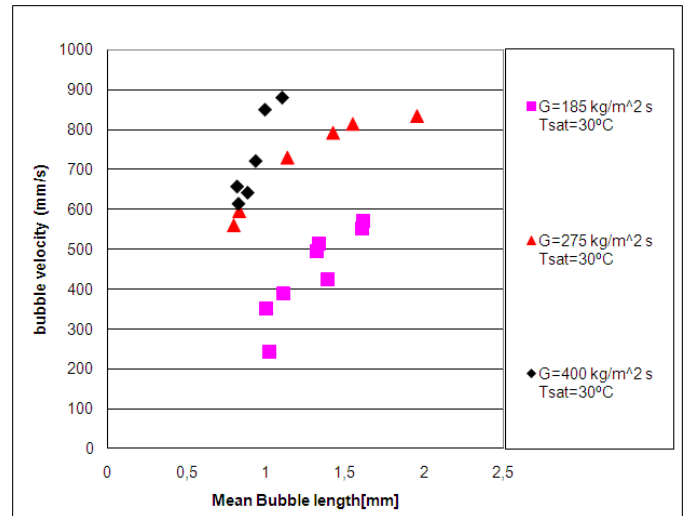


Fig 10 Variation of mean velocity and mean length of elongated bubbles, $T_{\text{sat}}=30 \text{ }^\circ\text{C}$

A relation between elongated bubble velocity and mean bubble length is shown in figure 10. For a given length of a bubble, the mean velocity is higher for a higher mass flux, as

expected. This will be explained by the fact that increasing the mass flux will increase the liquid and vapor relative velocities in a two-phase flow. Bubble velocity also increases with mean bubble length for a given mass flux. A change in slope for a mass flux of $G=275 \text{ kg/m}^2 \text{ s}$, may probably indicate a tendency towards the change of flow regime due to increased merger rate because of increased velocity of bubbles as discussed earlier in this section.

CONCLUSION

Visualization experiments in a microchannel of 0.781 mm internal diameter were conducted to understand the basic physics involved in two-phase flow and to explore the effects of mass flux, heat flux, system pressure and vapour quality on the flow patterns and bubble behaviour. A single circular, horizontal, transparent microchannel made of fused silica was used with a uniformly heated length of 191 mm and using refrigerant R-134a as working fluid. Outside of the test tube was coated with a thin electrically conductive layer of ITO which allowed simultaneous heating and visualization. The experimental results show several interesting phenomena during flow boiling in a microchannel. Some major findings are summarised below:

Notably, the bubbles generated in the current study were due to the nucleation of natural cavities present in the tube surface in contrary to many flow visualization studies of air-water systems present in the literature.

Major flow patterns observed during boiling process were: Isolated bubble, Confined bubble, elongated bubble, slug flow, semi annular and annular flow.

Small channel diameter was observed to restrict the bubble growth and was thus, responsible for early transition from confined bubbly to elongated bubble flow pattern.

Early transition to elongated bubble caused early transition to slug flow and annular flow regimes. This is an interesting phenomenon which might be a reason for early occurrence of annular flow (i.e. at low vapour fractions) in microchannels.

Increased heat flux caused vigorous boiling and activated more nucleation sites available on the channel surface.

Bubble frequency was observed to increase with both heat and mass flux. Increased bubble frequency caused an increase in coalescence rate. Increased coalescence rate was also observed for increased mass fluxes (the higher the mass flux, higher will be the vapour velocity) which might be responsible for early transition to annular flow for higher mass fluxes.

Bubble diameter after detachment was observed to be smaller for a higher mass flux.

A relationship between the mean bubble length and mean bubble velocity shows that increase in both the parameters will ultimately lead to increased merger rate of the elongated bubbles and transition to successive flow regime.

More flow visualization studies with wide operating conditions are still needed to understand the basic phenomena involved during two-phase flow in microchannels.

NOMENCLATURE

A	heat transfer area (m^2)
A_c	cross sectional area (m^2)
C_p	specific heat (J/kg K)
D	diameter (m)
f	friction factor
G	mass flux ($\text{kg/m}^2 \text{ s}$)
I	current (A)
i_{lg}	latent heat of vaporization (J/kg)
L	length (mm)
m	mass flow rate of refrigerant (kg/s)
P	pressure (bar)
P	Pixels
Q	power (W)
q''	heat flux (W/m^2)
T	temperature ($^\circ\text{C}$)
t	time (second)
V	voltage (V)
v	velocity (mm/s)
x_{th}	thermodynamic vapor quality (-)
z	Length, axial position (m)

Greek letters

μ	dynamic viscosity (Ns/m^2)
ΔP	pressure loss (mbar)
ΔT_{sub}	subcooling degree, $T_{sat}-T_{in}$ ($^\circ\text{C}$)

Subscripts

exp	experimental
f	final
g	gas
h	heated
i	initial
in	inlet
l	liquid
m	momentum
ref	reference
sat	saturation
sp	single phase
tot	total
tp	two-phase

Dimensionless numbers

Re	Reynolds number $\frac{GD}{\mu_l}$
------	------------------------------------

REFERENCES

- [1] Palm. B, 2001, Heat Transfer in Microchannels, *Microscale Thermophysical Engineering.*, 5(3) pp. 155-175.
- [2] Kuo. C.J, Kosar. A, Peles. Y, Virost. S, Mishra. C and Jensen. M.K, 2006, Bubble dynamics during boiling in enhanced surface microchannels, *J. Microelectromechanical systems.*, 15 pp. 1514-1527.
- [3] Revellin. R, Agostini. B, Ursenbacher. T, and Thome. J.R, 2008, Experimental investigation of velocity and length of elongated bubbles for flow of R-134a in a 0.5 mm microchannel, *Exp. Thermal Fluid Science.*, 32 pp. 870-881.
- [4] Owhaib. W, Palm. B and Martin-Callizo. C, 2007, A visualization study of bubble behaviour in saturated flow boiling through a vertical mini-tube. *J. Heat Transfer Engineering.*, 28 pp. 852-860.
- [5] Celata. G.P, Cumo. M, Gervasi. M and Zummo. G, 2006, Flow pattern analysis of flow boiling in microgravity, *ECI International Conference on Boiling Heat Transfer.*, May 7-12, Spoleto, Italy.
- [6] Coleman. J.W and Garimella. S, 1999, Characterization of two-phase flow patterns in small diameter round and rectangular tubes, *Int. J. Heat Mass Transfer.*, 42 pp. 2869-2881.
- [7] Yang. Z.L, Palm. B and Sehgal. B.R, 2002, Numerical simulation of bubbly two-phase flow in a narrow channel, *Int. J. Heat Mass Transfer.*, 45 pp. 631-639.
- [8] Bretherton. F.P, 1960, The motion of long bubbles in tubes, *J. Fluid Mech.*, 10 pp. 166-188.
- [9] Han. Y, and Shikazono. N, 2009, Measurement of the liquid film thickness in micro tube slug flow, *Int. J. Heat Fluid Flow.*, 30 pp. 842-853.
- [10] Han. Y, and Shikazono. N, The effect of bubble acceleration on liquid film thickness in micro tubes, *Int. J. Heat Fluid Flow.*, Article in press.
- [11] Collier. J.G and Thome. J.R, 1994, Convective boiling and condensation, *3rd Edition* Oxford Science Publications, pp 184.
- [12] NIST, National Institute of Standard and Technology, REFPROP Version 7.0 (2002), Boulder Colorado.
- [13] Moffat. R.J, 1988, Describing the uncertainties in experimental results, *Exp. Therm. Fluid Science.*, 1 pp. 3-17.
- [14] Triplett. K.A, Ghiaasiaan. S.M, Abdel-Khalik. S.I and Sadowski. D.L, 1999, Gas-liquid two-phase flow in microchannels Part I: Two-phase flow patterns, *Int. J. Multiphase flow.*, 25 pp. 377-394.
- [15] Martin-Callizo. C, Palm. B, Owhaib. W and Ali. R, 2010, Flow boiling visualization of R134a in a vertical channel of small diameter, *ASME J. Heat Transfer.*, 132.
- [16] Huo. X, Chen. L, Tian. Y.S and Karayiannis. T.G, 2004, Flow boiling and flow regimes in small diameter tubes, *Applied Thermal Engineering.*, 24 pp. 1225-1239.
- [17] Revellin. R and Thome. J.R, 2007, Experimental investigation of R-134a and R245fa two-phase flow in microchannels for different flow conditions, *Int. J. Heat Fluid Flow.*, 28 pp. 63-71.
- [18] Steinke. M.E, Kandlikar. S.G, 2004, An experimental investigation of flow boiling characteristics of water in parallel microchannels, *ASME J. Heat Transfer.*, 126 pp. 518-526.
- [19] Owhaib. W, 2007, Experimental heat transfer, pressure drop, and flow visualization of R134a in vertical mini/micro tubes, *Doctoral Thesis, Department of Energy Technology, Royal Institute of Technology.*
- [20] Agostini. B, Revellin. R and Thome. J.R, 2008, Elongated bubbles in microchannels Part I: Experimental study and modelling of elongated bubble velocity, *Int. J. Multiphase flow.*, 34 pp. 590-601.